Astronomy & Astrophysics

Revisiting the birth locations of pulsars B1929+10, B2020+28, and B2021+51

Franz Kirsten[1,2,3,★], Wouter Vlemmings[4], Robert M. Campbell[5], Michael Kramer[2], and Shami Chatterjee[6]

[1] International Centre for Radio Astronomy Research (ICRAR), Curtin University, GPO Box U1987, Perth, WA 6845, Australia
e-mail: franz.kirsten@curtin.edu.au
[2] Max Planck Institut für Radioastronomie (MPIfR), Auf dem Hügel 69, 53121 Bonn, Germany
[3] Argelander Institut für Astronomie (AIfA), Universität Bonn, Auf dem Hügel 71, 53121 Bonn, Germany
[4] Department of Earth and Space Sciences, Chalmers University of Technology, Onsala Space Observatory, 439 92 Onsala, Sweden
[5] Joint Institute for VLBI in Europe, Oude Hoogeveensedijk 4, 7991 PD Dwingeloo, The Netherlands
[6] Department of Astronomy, Cornell University, Ithaca, NY 14853, USA

ABSTRACT

We present new proper motion and parallax measurements obtained with the European VLBI Network (EVN) at 5 GHz for the three isolated pulsars B1929+10, B2020+28, and B2021+51. For B1929+10 we combined our data with earlier VLBI measurements and confirm the robustness of the astrometric parameters of this pulsar. For pulsars B2020+28 and B2021+51 our observations indicate that both stars are almost a factor of two closer to the solar system than previously thought, placing them at a distance of $1.39^{+0.05}_{-0.06}$ and $1.25^{+0.14}_{-0.17}$ kpc. Using our new astrometry, we simulated the orbits of all three pulsars in the Galactic potential with the aim to confirm or reject previously proposed birth locations. Our observations ultimately rule out a claimed binary origin of B1929+10 and the runaway star ζ Ophiuchi in Upper Scorpius. A putative common binary origin of B2020+28 and B2021+51 in the Cygnus Superbubble is also very unlikely.

Key words. pulsars: individual: B1929+10 – pulsars: individual: B2020+28 – pulsars: individual: B2021+51 – parallaxes – techniques: interferometric – proper motions

1. Introduction

Typical transverse velocities of isolated pulsars are of the order of several hundred km s^{-1} (Cordes & Chernoff 1998; Arzoumanian et al. 2002; Hobbs et al. 2005), while those of their progenitor O- and B-stars are at most several tens of km s^{-1}. In the standard neutron star formation scenario this discrepancy is explained by an asymmetry in the supernova (SN) explosion that imparts a kick to the forming central compact object, accelerating it to the observed velocities (e.g. Scheck et al. 2006). As a result of the short lifetime of SN remnants ($<10^5$ yr) and the typical characteristic age of young pulsars ($\tau_c \sim 10^{6-7}$ yr), direct associations between SN-remnants and pulsars are rare. Measurements of accurate proper motions μ and parallaxes π of pulsars can, however, indicate the birth locations of pulsars. The combination of both μ and the distance $d = 1/\pi$ yields the physical transverse velocity, $V_\perp$, which, given an estimate of the radial velocity, V_r, allows calculating a trajectory that traces the pulsar back to its possible birth location. Hence, kinematic ages – as opposed to characteristic ages $\tau_c = P/2\dot{P}$ – of pulsars can be determined and conclusions about neutron star formation scenarios can be drawn.

One of the first to calculate pulsar orbits was Wright (1979), claiming that the pulsars B1929+10 (J1932+1059) and B1952+29 originate from a former binary system. More recently, Hoogerwerf et al. (2001) used the 3D space velocity of high-velocity runaway stars and parallax and proper motion measurements of young nearby pulsars to extrapolate their trajectories back in time. Their simulations indicated that the runaway O-star ζ Ophiuchi (ζ Oph, HIP 81377) and the young pulsar B1929+10 were likely to have been in a binary system in Upper Scorpius (Scorpius-Centaurus association) until about 1 Myr ago. According to their analysis, the system was disrupted when the progenitor star underwent a supernova explosion. During that event, the space velocity vectors of both ζ Oph and the pulsar were modified to point away from Upper Scorpius. The parameter range for which such a scenario is possible is, however, rather small. Improved measurements of μ and π for B1929+10 obtained with the NRAO Very Long Baseline Array (VLBA) led to the conclusion that a common origin of the pulsar and ζ Oph is unlikely (Chatterjee et al. 2004). Adopting the measurements of Chatterjee et al. (2004), but increasing the reported uncertainties by factors between 10 and 30, Bobylev (2008) and also Tetzlaff et al. (2010) repeated the simulations of Hoogerwerf et al. (2001), re-postulating a binary origin of B1929+10 and ζ Oph in Upper Scorpius.

In a similar investigation, Vlemmings et al. (2004) identified the two pulsars B2020+28 and B2021+51 as candidates for a common-origin scenario based on proper motion and parallax measurements obtained with the VLBA at 1.4 GHz (Brisken et al. 2002). The authors simulated the trajectories of the two pulsars back in time and concluded that they most likely originated from a binary system in the Cygnus Superbubble that was disrupted when the younger of the two pulsars was born in a supernova. The measurements by Brisken et al. (2002) are, however,

---

Table 1. Observing epochs and arrays.

Date(s)	UT range	Array[a]												
2010 May 28-29	2130–0930	Ef	Wb	Jb	Jv	On	Mc	Tr			Zc	Bd	Ur	Sh
2010 Oct. 27	1130–2330	Ef	Wb			On	Mc	Tr	Ys	Sv	Zc	Bd		
2011 Mar. 09	0300–1500	Ef	Wb	Jb	Jv	On	Mc	Tr	Ys	Sv	Zc	Bd	Ur	Sh
2011 Jun. 01-02	2120–0920	Ef	Wb	Jb		On		Tr	Ys	Sv	Zc	Bd	Ur	Sh

Notes. [a] Ef = Effelsberg, DE, 100 m; Wb = Westerbork Synthesis Radio Telescope, NL, $12 - 14 \times 25$ m; Jb = Jodrell Bank Lovell Telescope, UK, 76 m; Jv = Jodrell Bank Mark2 Telescope, UK, 25 m; On = Onsala, SE, 25 m; Mc = Medicina, IT, 32 m; Tr = Torun, PL, 32 m; Ys = Yebes, ES, 40 m; Sv = Svetloe, RU, 32 m; Zc = Zelenchukskaya, RU, 32 m; Bd = Badary, RU, 32 m; Ur = Urumqi, CN, 32 m; Sh = Shanghai, CN, 25 m.

Table 2. Calibrator details for each pulsar.

Source	Pointing centre		Distance to pulsar [deg]	Flux density[b] [mJy beam^{-1}]
	RA	Dec		
B1929+10	19:32:14.0160	10:59:32.868		50
J1928+0848[a]	19:28:40.8555	08:48:48.413	2.35	160
J1934+1043	19:34:35.0256	10:43:40.366	0.63	50
B2020+28	20:22:37.0697	28:54:22.976		30
J2020+2826[a]	20:20:45.8707	28:26:59.195	0.61	70
J2023+3153	20:23:19.0173	31:53:02.306	2.98	900
B2021+51	20:22:49.8596	51:54:50.400		80
J2025+5028[a]	20:25:24.9725	50:28:39.536	1.49	110
J2023+5427	20:23:55.8440	54:27:35.829	2.55	500

Notes. [a] These are the calibrators referred to as primary calibrators in the text. [b] For the pulsars this is the apparent pulsar flux density measured by employing pulse gating.

based on five observations covering a time span of only roughly one year.

Here, we present new measurements of μ and π for the three pulsars B1929+10, B2020+28, and B2021+51 obtained with the European VLBI Network (EVN) at an observing frequency of 5 GHz. These observations extend the time baseline to more than ten years, allowing for an extremely high precision in measurements of μ and π for all three pulsars. We used these data and ran new simulations of trajectories to shed new light on the proposed binary origin of B1929+10/ζ Oph and B2020+28/B2021+51.

2. Observations and data reduction

The observations described here were conducted with the EVN under project code EV018(A-D). All observations used a frequency range 4926.49−5054.49 MHz with dual circular polarizations and two-bit sampling, for a total bit-rate of 1 Gbps per station. The 128 MHz frequency range in each polarization was split into eight 16 MHz baseband channels. We conducted four epochs of observations between May 2010 and June 2011, as summarized in Table 1. This table also lists the EVN stations that successfully participated in the array at each epoch.

We observed each of the three pulsars in all four 12-h epochs, using phase-referencing. Table 2 summarizes the pulsars and characteristics of their phase-reference calibrator sources. Our phase-referencing tactics included (i) a basic four-minute cycle alternating between the target pulsar (2.5 min) and the primary calibrator (1.5 min); and (ii) insertion of an additional 1.5 min scan of the secondary calibrator in every second cycle. For bandpass calibration, we observed the quasars J1800+3848 and 3C 454.3: the former about two hours from the beginning and the latter four hours from the end of each epoch. This observing pattern provides about two hours of integration on each

pulsar per epoch, yielding a nominally expected sensitivity of the arrays ranging from 10.9 to 14.8 μJy per beam.

The data from the telescopes were correlated on the EVN software correlator at the Joint Institute for VLBI in Europe (SFXC; Keimpema et al. 2015). Each of the 16 MHz baseband channels was correlated with 32 frequency points and one-second coherent integrations. Pulsar scans were correlated using the gating/binning capability of SFXC. Because these were the first observations to employ this mode, we devote a few sentences to describe it. Given an ephemeris of a pulsar, SFXC can apply a gate, defined by a start and stop fraction of a period, such that correlation accumulates only during the in-gate interval. Before gating, the pulsar data are de-dispersed. Here, we used incoherent de-dispersion (a constant correction per 0.5 $\sim$ MHz frequency point). Coherent de-dispersion has subsequently been developed on SFXC. The gate itself may be divided further into a number of equal-width bins, each of which produces independent correlator output. In this case, there was only one bin. In this way, assuming the entire pulse falls within the gate, the signal-to-noise ratio (S/N) of the pulsar detections can be increased by a factor of about $\sqrt{P/w}$, where P is the pulse period and w is the width of the gate. The pulsar ephemerides were derived with TEMPO2[1] (Hobbs et al. 2006). Before full correlation, we conducted iterations of gate-fitting, using a full-period gate with 40 bins, to confirm that the pulse profile was stationary over the time-range of a pulsar observation within an epoch and to optimize the choice of the gate start/stop parameters. For these three pulsars, the gate widths used were typically in the range of 4−8% of a pulse period, leading to gating gain factors of ∼3−5.

We performed a mostly automated data reduction and calibration procedure relying on the NRAO Astronomical Image Processing System (AIPS) and the scripting language

---

[1] http://www.atnf.csiro.au/research/pulsar/tempo2/

ParselTongue (Kettenis et al. 2006). Removal of data affected by radio frequency interference (RFI) was made running the RFI-mitigation software SERPent (Peck & Fenech 2013) and some further manual flagging. We first applied the system temperature and gain curve corrections as determined by the EVN pipeline[2] and also corrected for the parallactic angle using the AIPS task CLCOR. Next we computed ionospheric corrections in TECOR with the help of total electron content maps as published by the Center for Orbit Determination in Europe[3]. In a first calibration run, we solved for visibility rates, phases, and delays in FRING for all calibrator sources assuming a simple point source model. Next, we self-calibrated on each source, improving the S/N by a factor of five to ten. For each calibrator we then concatenated the calibrated data from all four epochs. This dataset was imaged to produce a global model of each calibrator source. The dominant CLEAN components of each source model were then used as the input model parameters in a second FRING-run. In this way, we eliminated any systematics caused by source structure that affected the position of the calibrator sources in between epochs. For each of the three pulsars the calibration solutions of the primary calibrator were of much higher quality than those of the secondary calibrator and, hence, were applied to the respective target pulsar (Table 2).

We used the calibration solutions from the secondary calibrator to provide independent checks on the achieved astrometric accuracy as a function of angular separation between target and calibrator source ("calibrator throw"), as done by Chatterjee et al. (2004). Similarly to the earlier data, our observations imply an almost linear increase in astrometric accuracy with decreasing calibrator throw (Fig. 1). We fitted a power law, $y = a \cdot x^b$, to all data points obtained from 5 GHz observations, which yielded $(a, b) = (0.15 \pm 0.09, 1.17 \pm 0.31)$. This relation, however, seems to only hold for angular separations of up to four degrees between calibrator and target.

3. Estimates for astrometric parameters of B1929+10, B2020+28, and B2021+51

We measured the position of the pulsars in each epoch by fitting a 2D Gaussian to the brightness distribution in the image plane (Fig. 2) using the AIPS task IMFIT. As a result of the high S/N (~150) and small beam size ($\theta \sim 3 \times 5$ mas), the formal errors are very small ($\theta/(2 * S/N) \sim 10 \times 20 \mu$as), certainly underestimating the real positional uncertainties. In addition to these random errors, residual systematic errors caused by the calibrator throw (Fig. 1), for instance, need to be taken into account. A good estimate for these systematic errors is the deconvolved size θ_d of the pulsar, which is zero for a true point source. Following the scheme reported in Chatterjee et al. (2001), we estimated the systematic uncertainties using the quantity $\theta_d / \sqrt{(N_{ant} - 1) * t_{obs}/t_{iono}}$, where $N_{ant} = 11$ is the typical number of antennas involved, $t_{obs} = 110$ min is the total amount of time spent on each pulsar, and $t_{iono} = 6$ min is the empirically determined atmospheric coherence time at 5 GHz. For the total positional uncertainty we added both the formal and the systematic errors in quadrature. Table 3 lists the measured positions of all three pulsars in the third epoch at MJD 55629.

To estimate each pulsar's proper motion and parallax, we performed a weighted least-squares-fit to the measured positions. Here, we measured both parameters in three ways: we
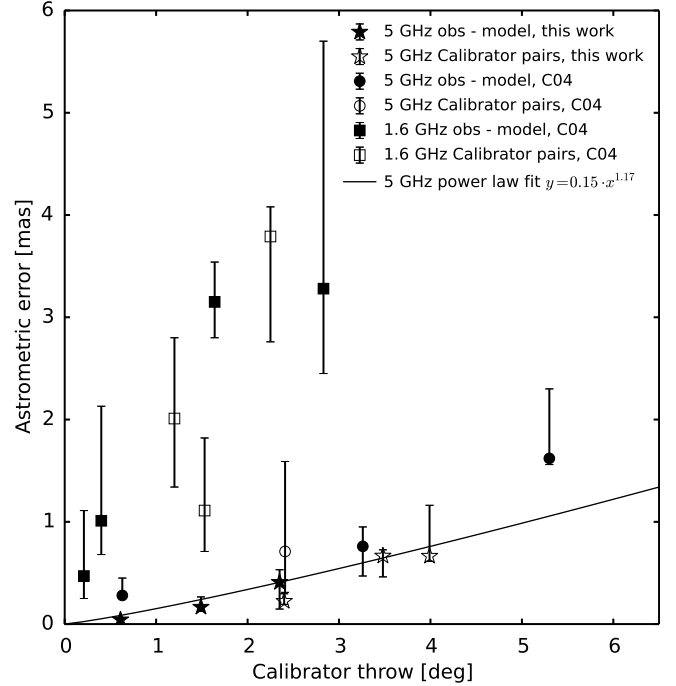

Fig. 1. Astrometric accuracy as a function of angular separation between phase calibrator source and target. This is a reproduction of Fig. 3 in Chatterjee et al. (2004) (referred to as C04 here) to which we added data from our observations (open and filled stars). Open symbols denote the median scatter about the average position of the primary phase calibrator obtained from calibrating its visibilities with solutions from the secondary calibrator. Filled symbols show the median scatter of the observed positions about the best-fit model for proper motion and parallax. The 1.6 GHz data (squares) are taken from Chatterjee et al. (2001) and Vlemmings et al. (2003), while the previous 5 GHz data (circles) are taken from Chatterjee et al. (2004). The solid line is a weighted least-squares power-law fit to all 5 GHz data points. The almost linear relationship between astrometric error and calibrator throw seems to break down beyond an angular separation of more than about four degrees.

considered our position measurements alone (Fig. 3), we combined our data with those of the publications listed in Table 4 (Fig. 4), and we employed a bootstrapping technique. For the latter, we randomly sampled the position measurements that are available for each individual pulsar. These positions were then fitted and the results were stored. This procedure was repeated 10^5 times, yielding distributions as shown in Fig. 5. During the fitting procedure we allowed for absolute positional offsets between the different data sets (typically of the order of several mas). Such offsets are expected for several reasons: i) the observations were conducted at different frequencies; ii) the different campaigns used different calibrator sources, which may have different systematic errors (e.g. Kovalev et al. 2008; Porcas 2009; Sokolovsky et al. 2011) in their ties to the International Celestial Reference Frame (ICRF2, Ma et al. 2009); iii) the data were obtained at times that are up to ten years apart during which improvements to the correlator models and Earth orientation parameters introduce offsets; and iv) the data were taken with different instruments (VLBA and EVN) that use different hardware/software correlators. Table 5 summarizes the estimates of μ and π from the individual fits, from the different combinations of data sets, and from the bootstrapping method (where we quote the most compact 68% confidence interval), as well as the implied pulsar distances and transverse velocities. The latter are corrected for solar motion and differential Galactic rotation and
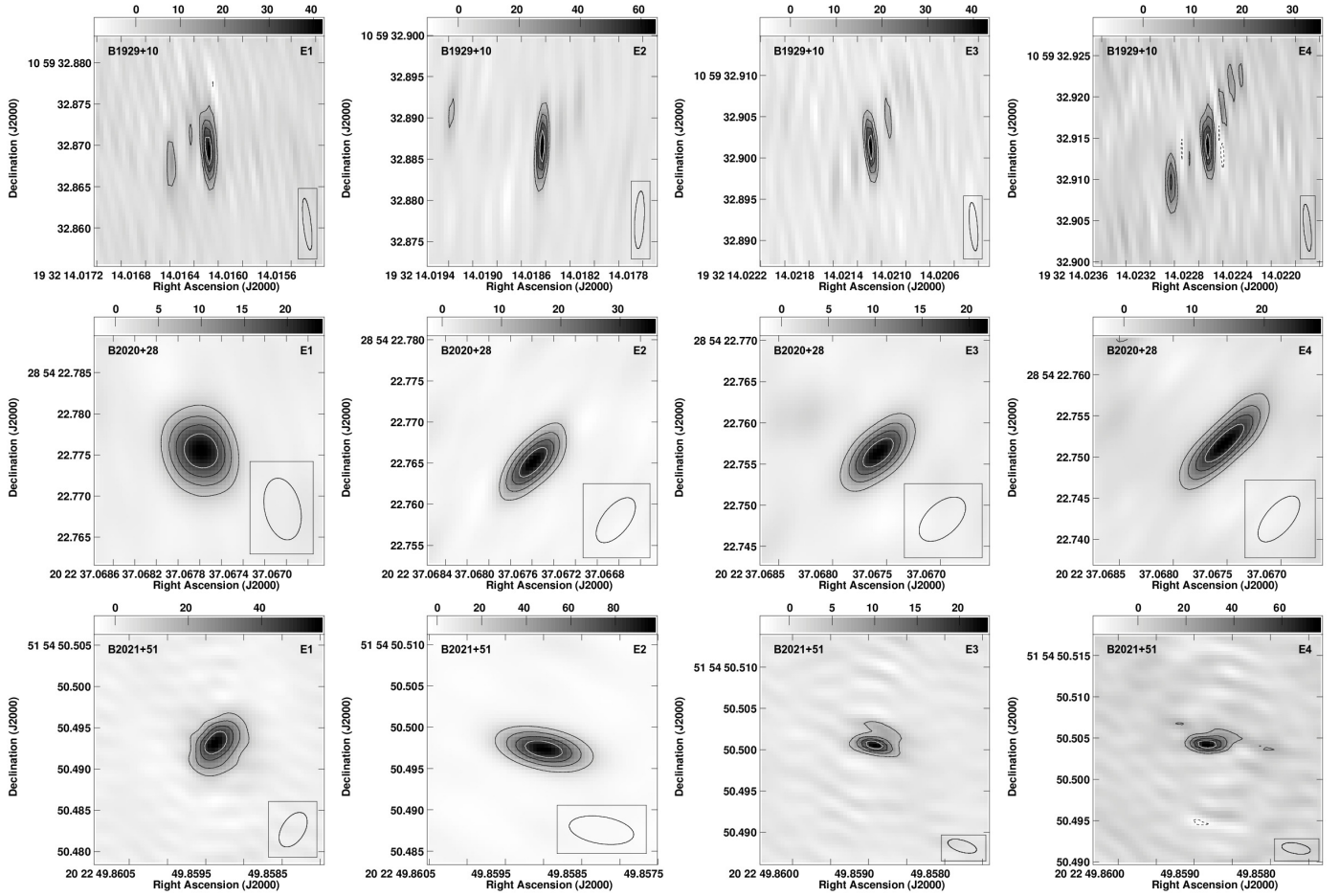
Fig. 2. Greyscale plots of the fitted pulsar images. Rows from *top to bottom* show B1929+10, B2020+28, and B2021+51. Columns from *left to right* correspond to epochs one to four. Overlaid contours increase in steps of 20 percent of the peak flux density, where negative values are indicated by dashed contours. The absolute flux density scale (mJy beam^{-1}) is indicated above each individual panel, and the beam size and position angle are indicated in the bottom right. The larger beam sizes for B2020+28 and B2021+51 compared to that of B1929+10 are due to flagging of baselines to Sh and/or Ur.

Table 3. Measured positions at MJD 55 629.

Pulsar	RA (J2000)	Dec (J2000)	S/N	Beam size [mas×mas]
B1929+10	19:32:14.021289(1)	10:59:32.90137(5)	155	1.01×5.94
B2020+28	20:22:37.06758(1)	28:54:22.7563(2)	142	3.76×7.36
B2021+51	20:22:49.85890(1)	51:54:50.5005(1)	156	1.72×3.97

Notes. Numbers in brackets indicate the uncertainty in the last digit. The larger beam size for B2020+28 is due to flagging of baselines to Sh and Ur.

refer to the local standard of rest (LSR). Regardless of estimation strategy and combination of available data, all measured values are consistent within their uncertainties at the one-sigma level.

For pulsar B1929+10 our results confirm the measurements of Chatterjee et al. (2004), especially in combination with the earlier data. For pulsars B2020+28 and B2021+51 our observations indicate that they are located at a distance of $1.39^{+0.05}_{-0.06}$ kpc and $1.25^{+0.14}_{-0.17}$ kpc. Hence, they are about 1.1 and 0.7 kpc closer to the solar system than what was implied by the measurements of Brisken et al. (2002) alone (Table 4). Considering this discrepancy of a factor of about 2, we suspect that the uncertainties on the position measurements for B2020+28 and B2021+51 as reported by the authors were underestimated. Accordingly, we did not include these data in the further analysis. Thus, in the following, for B1929+10 we adopted the astrometric

parameters obtained from bootstrapping all available data, while for B2020+28 and B2021+51 we used the parameters as measured with our new 5 GHz data alone. Hence, the analysis below is based on the astrometry as listed in Table 6.

4. Simulations of pulsar orbits

To shed new light on possible common origins of B1929+10/ζ Oph and B2020+28/B2021+51, we used the pulsar astrometric parameters described above and traced their orbits back in time through the Galactic potential. For the runaway star ζ Oph we used the latest proper motion and parallax measurements from van Leeuwen (2007) (Table 6) and adopted the value for the radial velocity $V_{\rm rad} = -9.0 \pm 5.5$ km s^{-1} from Kharchenko et al. (2007). Our astrometric measurements yield information

Table 4. Previous proper motion and parallax estimates and derived values.

Pulsar	μ_α [mas yr^{-1}]	μ_δ [mas yr^{-1}]	π [mas]	d [kpc]	$V_\perp$ [km s^{-1}]	Reference
B1929+10	99.0 ± 12.0	39.0 ± 8.0	4.00 ± 2.0	$0.24^{+0.09}_{-0.12}$	124^{+140}_{-52}	1
B1929+10	94.82 ± 0.26	43.04 ± 0.15	3.02 ± 0.09	$0.33^{+0.01}_{-0.01}$	162^{+6}_{-5}	2
B1929+10	94.09 ± 0.11	42.99 ± 0.16	2.77 ± 0.07	$0.361^{+0.009}_{-0.009}$	176^{+5}_{-5}	3
B2020+28	-4.38 ± 0.53	-23.59 ± 0.26	0.37 ± 0.12	$2.70^{+0.64}_{-0.96}$	256^{+135}_{-62}	2
B2021+51	-5.23 ± 0.17	11.54 ± 0.28	0.50 ± 0.07	$2.00^{+0.23}_{-0.31}$	149^{+28}_{-22}	2

References. (1) Hoogerwerf et al. (2001); (2) Brisken et al. (2002); (3) Chatterjee et al. (2004).

Table 5. Astrometric results and derived values from the estimation strategies.

Pulsar	Data sets[a] F[b]	B[c]	N_{obs}	μ_α [mas yr^{-1}]	μ_δ [mas yr^{-1}]	π [mas]	χ^2_{red}	d [kpc]	$V_\perp$ [km s^{-1}]
B1929+10	C		4	94.11 ± 0.52	43.64 ± 1.06	2.79 ± 0.14	1.34	$0.358^{+0.017}_{-0.019}$	175^{+11}_{-10}
	C_C, C		10	94.04 ± 0.12	43.39 ± 0.23	2.79 ± 0.08	1.03	$0.358^{+0.010}_{-0.010}$	175^{+5}_{-5}
	L, C		9	94.20 ± 0.20	42.93 ± 0.26	2.78 ± 0.05	0.51	$0.360^{+0.006}_{-0.006}$	175^{+4}_{-3}
	L, C_C, C		15	94.06 ± 0.09	43.24 ± 0.17	2.78 ± 0.06	0.77	$0.360^{+0.007}_{-0.008}$	176^{+4}_{-5}
		C_C, C	10	$94.07^{+0.14}_{-0.20}$	$43.41^{+0.10}_{-0.12}$	$2.76^{+0.10}_{-0.14}$		$0.362^{+0.019}_{-0.012}$	177^{+7}_{-7}
		L, C	9	$94.23^{+0.14}_{-0.24}$	$42.95^{+0.23}_{-0.26}$	$2.79^{+0.07}_{-0.12}$		$0.362^{+0.019}_{-0.012}$	175^{+8}_{-5}
		L, C_C, C	15	$94.08^{+0.13}_{-0.17}$	$43.25^{+0.16}_{-0.13}$	$2.77^{+0.08}_{-0.07}$		$0.361^{+0.009}_{-0.010}$	176^{+5}_{-5}
B2020+28	C		4	-3.34 ± 0.05	-23.65 ± 0.11	0.72 ± 0.03	0.05	$1.39^{+0.05}_{-0.06}$	134^{+6}_{-6}
	L, C		9	-3.46 ± 0.17	-23.73 ± 0.21	0.61 ± 0.08	0.53	$1.63^{+0.18}_{-0.23}$	158^{+25}_{-20}
		L, C	9	$-3.45^{+0.16}_{-0.33}$	$-23.70^{+0.32}_{-0.22}$	$0.60^{+0.13}_{-0.14}$		$1.66^{+0.50}_{-0.29}$	160^{+50}_{-30}
B2021+51	C		4	-5.08 ± 0.42	10.84 ± 0.25	0.80 ± 0.11	1.54	$1.25^{+0.14}_{-0.17}$	87^{+15}_{-12}
	L, C		9	-5.03 ± 0.27	10.96 ± 0.17	0.78 ± 0.07	0.90	$1.28^{+0.10}_{-0.12}$	90^{+11}_{-9}
		L, C	9	$-5.01^{+0.17}_{-0.20}$	$10.99^{+0.18}_{-0.29}$	$0.77^{+0.08}_{-0.10}$		$1.30^{+0.19}_{-0.13}$	91^{+16}_{-12}

Notes. [a] C refers to the measurements obtained in this campaign, C_C denotes the data set from Chatterjee et al. (2004), and L indicates that the measurements from Brisken et al. (2002) were included in the analysis. [b] Results derived from a least-squares fit of the measured data. [c] Median values and 68% confidence interval from fitting 10^5 bootstrapped realizations of the data.

about the transverse motion of the pulsars, but they do not contain any information about the radial velocity. To estimate the full 3D velocity vector, we simulated the possible radial component from our measured transverse components and the space velocity distribution of young pulsars as empirically derived by Hobbs et al. (2005). To account for the uncertainties of the measured parameters μ_α, μ_δ, π, and the unknown radial velocity, we assumed that all parameters are distributed normally (where the half-width of the Gaussian is given by the higher absolute value of the upper and lower errors of the bootstrapping results) and performed three million Monte Carlo simulations. The obtained velocity vectors were corrected for the solar motion with respect to the LSR, for differential Galactic rotation, and also for the velocity of the LSR. The Galactic potential we used in our simulations is the potential that was described in full detail in Vlemmings et al. (2004), the main parameters of which we summarize here in brief. For consistency reasons, the pulsar orbits were traced back through the same Stäckel potential as in Vlemmings et al. (2004); consisting of a thin disk, a thick disk, and a halo component whose axis ratios are 75.0, 1.5, and 1.02,

respectively. We kept the relative contributions of thin and thick disks and of the halo at 0.13, 0.01, and 1.0, respectively. For a complete description of each parameter of the Stäckel potential, we refer to Famaey & Dejonghe (2003). We adopted parameters for solar motion from Schönrich (2012): $R_\odot$ = 8.27 kpc and $(U, V, W) = (13.84, 12.24, 6.1)$ km s^{-1}. Each object's trajectory was sampled at time intervals of 10^3 yr using a fourth-order Runge-Kutta numerical integration method. For each time step the distances between the two objects under consideration were computed within the Galactic reference frame, and we recorded only the simulation input parameters of trajectories that resulted in a minimum distance of less than 10 pc. In addition to the separation between the individual objects, we also computed their distances to the Sun (B2020+28/B2021+51) and to the Upper Scorpius region (B1929+10/ζ Oph). To compute the latter, we traced the trajectory of Upper Scorpius back in time using the astrometric values as listed in Table 2 of de Zeeuw et al. (1999).

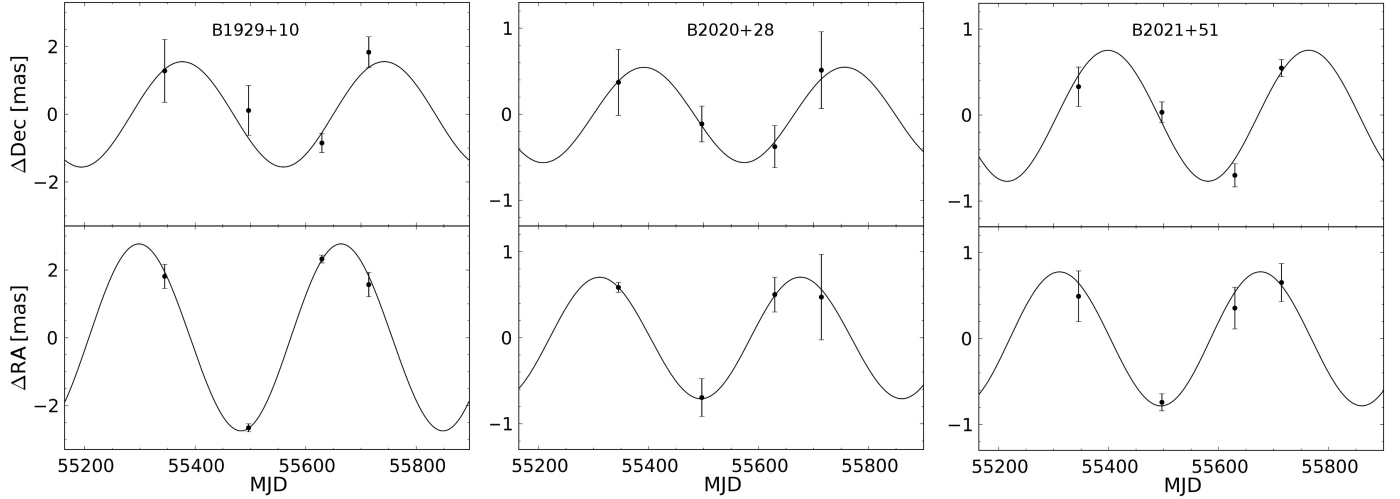For consistency checks we used the input parameters of Hoogerwerf et al. (2001) to compute the trajectories of

Fig. 3. Relative measured positions of B1929+10 (*left*), B2020+28 (*middle*), and B2021+51 (*right*) with the best-fit proper motion removed. The solid line is the best-fit parallax from our EVN 5 GHz observations.
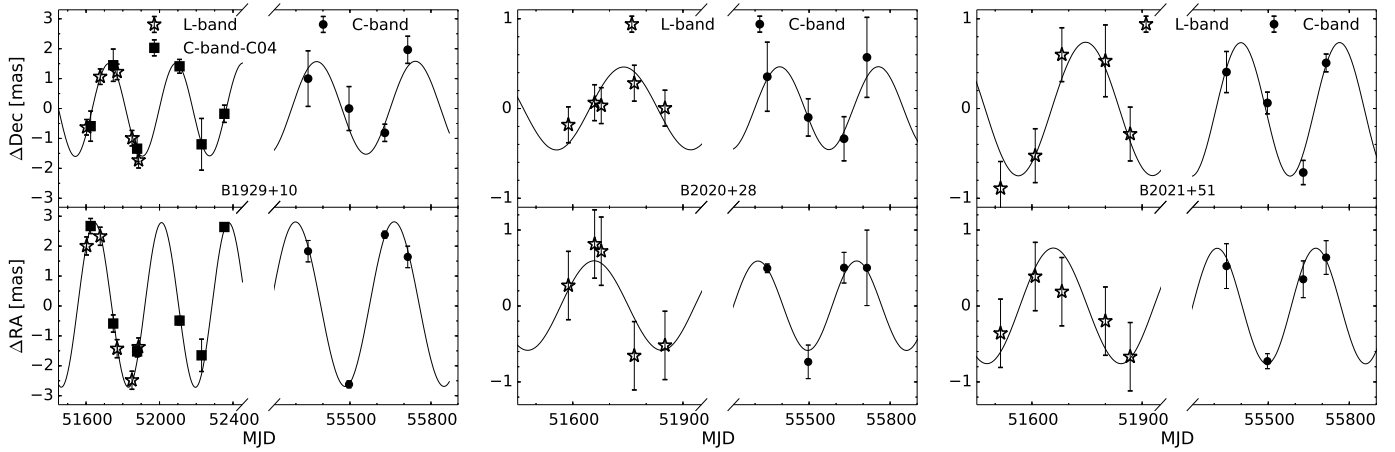

Fig. 4. Same as Fig. 3, but for the fits performed using all available data. Solid dots show the most recent measurements at 5 GHz, open stars are the data taken from Brisken et al. (2002), and squares are the data adopted from Chatterjee et al. (2004). For better illustration, we omitted the time span without any observations.

Table 6. Astrometric parameters used in the simulations.

Source	μ_α [mas yr^{-1}]	μ_δ [mas yr^{-1}]	π [mas]
B1929+10	94.08 ± 0.17	43.25 ± 0.16	2.77 ± 0.08
ζ Oph^a	15.26 ± 0.26	24.79 ± 0.22	8.91 ± 0.20
B1952+29^b	−30 ± 6	−34 ± 8	1.4 ± 1.0
B2020+28	−3.34 ± 0.05	−23.65 ± 0.11	0.72 ± 0.03
B2021+51	−5.08 ± 0.42	10.84 ± 0.25	0.80 ± 0.11

Notes. $^{(a)}$ From van Leeuwen (2007). $^{(b)}$ Proper motion from Hobbs et al. (2004), parallax from the ATNF Pulsar Catalogue (Manchester et al. 2005).

B1929+10 and ζ Oph. In total, 37 521 of the three million sampled trajectories (1.2%) cross within 10 pc of each other. This is close to the percentage found in Hoogerwerf et al. (2001): 30822 out of three million, or 1.0%. The smallest separation we found is 0.19 pc (compared to 0.35 pc). Furthermore, while Hoogerwerf et al. (2001) reported that in 4214 (0.14%) simulations the trajectories of both the pulsar and the runaway star not only pass within 10 pc of each other, but also pass within

less than 10 pc of Upper Scorpius, we found that 6816 (0.23%) of our simulations meet these conditions. The differences in the results are probably due to the different set-ups of the Galactic potentials. We did reproduce the general trend found by Hoogerwerf et al. (2001), however. When we ran the simulations using the same input parameters for B1929+10 as Hoogerwerf et al. (2001), but used the latest parameters for ζ Oph from van Leeuwen (2007), a total of 82840 (2.7%) simulated orbits cross within 10 pc, in only 8 of which both the pulsar and the star are less than 10 pc away from Upper Scorpius.

To test how much the updated solar parameters and the different radial velocity distributions[4] influence the computed trajectories, we also ran the simulations for B2020+28/B2021+51 using the input parameters for μ_α, μ_δ, and π from Vlemmings et al. (2004) (Table 4). In our simulations 0.14% of trajectories cross within 10 pc (minimal distance of 0.10 pc), reproducing the results of these earlier simulations well.

In the three million simulations that we ran using our bootstrapping results for B1929+10 and the latest astrometric

---

[4] We used a one-component velocity distribution, while Vlemmings et al. (2004) used a two-component distribution.
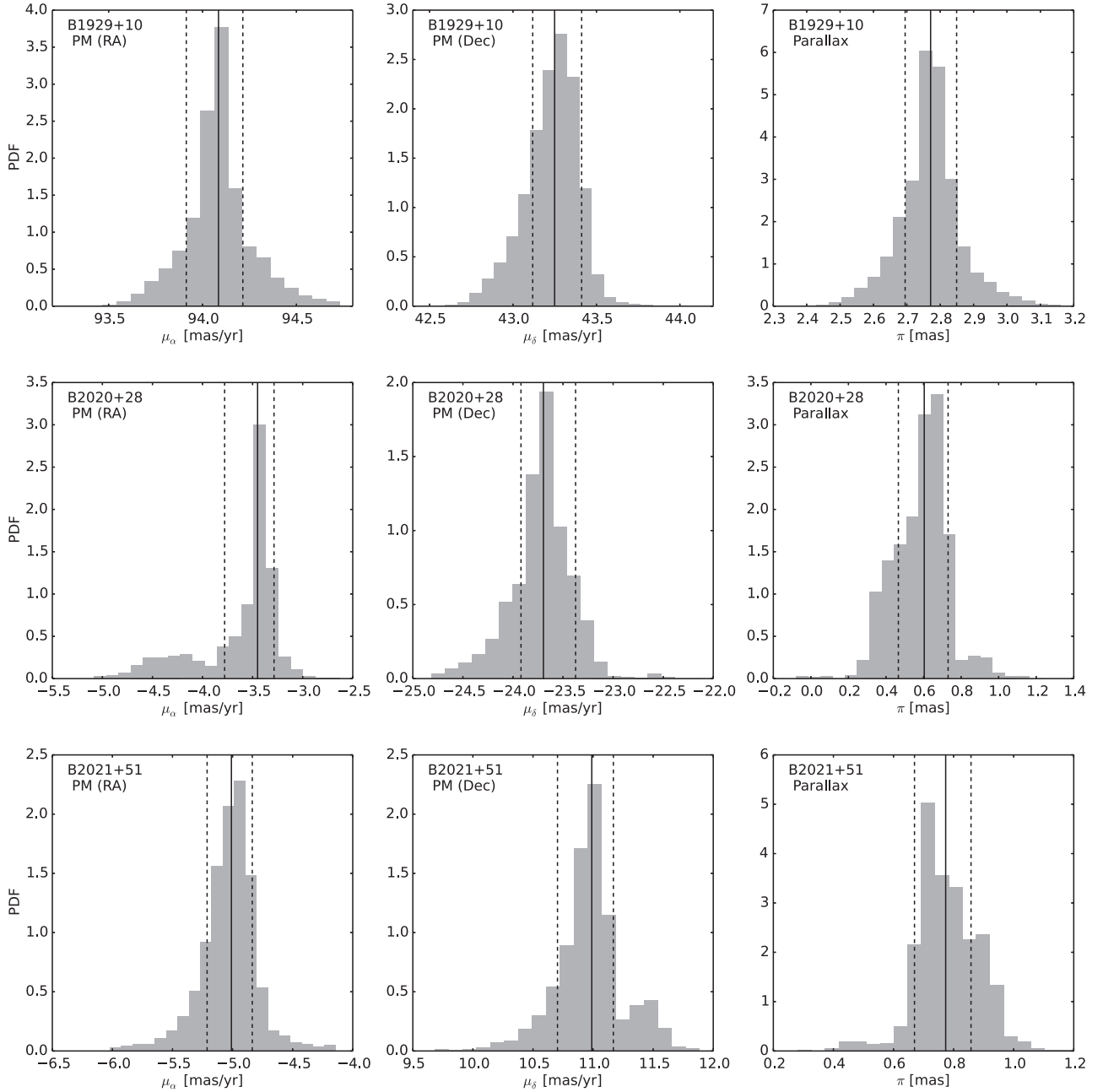
Fig. 5. Probability density functions of fitting results from bootstrapping all available data. *From top to bottom*: B1929+10, B2020+28, and B2021+51. Columns are from *left to right*: proper motion in RA, proper motion in Dec, and parallax. The solid and dashed vertical lines indicate the median and the most compact 68% confidence intervals as listed in Table 5.

parameters for ζ Oph, 258272 (8.6%) orbits cross within 10 pc about 0.5 Myr ago (Fig. 6). However, none of these orbits yield a minimum separation of less than 2.4 pc, and neither the pulsar nor the runaway star approach the centre of Upper Scorpius to within less than 17 pc. The median radial velocity of B1929+10 required for it to approach ζ Oph within 10 pc is 570^{+53}_{-63} km s^{-1} (Fig. 7). For completeness, we also tested the hypothesis that B1929+10 once formed a binary system with the pulsar B1952+29 (Wright 1979). For the latter we assumed the proper motion from Hobbs et al. (2004) and the parallax from the distance derived from the dispersion measure (DM) in the ATNF Pulsar Catalogue[5] and the Galactic electron density model from

Cordes & Lazio 2003 (Table 6). We assumed a parallax uncertainty of 1 mas in lieu of a formal error estimate in the DM-based distance. With these parameters, none of the simulated orbits crosses within 10 pc. The same is true for simulations ran with the same proper motion parameters, but with the distance estimate $d = 0.42$ kpc, based on the same DM but using instead the Galactic electron density model from Taylor & Cordes (1993).

For the putative pulsar pair B2020+28/B2021+51 our new measurements imply a minimum possible separation of 1.9 pc. Of the three million trajectories, 1866 (0.06%) cross within 10 pc about $1.16^{+0.18}_{-0.17}$ Myr ago (Fig. 6). The implied median radial velocities are 643^{+193}_{-168} for B2020+28 and 433^{+154}_{-193} km s^{-1} for B2021+51 (Fig. 7).
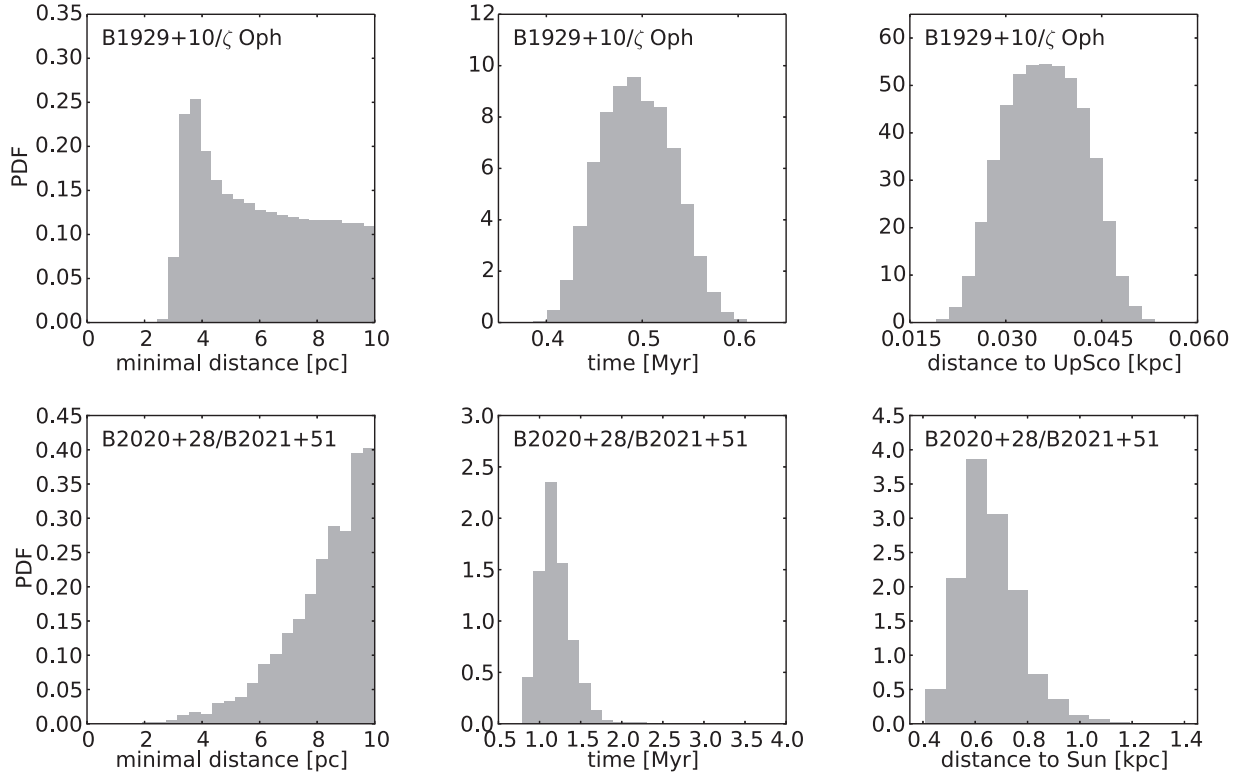

Fig. 6. Probability density functions of minimal distances (*left column*), time of minimal approach (*middle column*), and distance to Upper Scorpius and the Sun for B1929+10/ζ Oph (*upper row*) and B2020+28/B2021+51 (*lower row*), respectively. The stellar pair to which the figures apply is indicated in the top of each panel.

5. Discussion

5.1. Binary companion of B1929+10

Our new astrometric results for the pulsar B1929+10 confirm the measurements of earlier VLBI campaigns (Brisken et al. 2002; Chatterjee et al. 2004), and in combination with the previous position measurements, we place robust constraints on the uncertainties of the proper motion parameters. Accordingly, for our adopted parallax $\pi = 2.77^{+0.07}_{-0.08}$ our values for the proper motion differ by more than 10σ from the parameter space that implies a common origin of B1929+10 and ζ Oph in Upper Scorpius in Hoogerwerf et al. (2001). Given the new astrometry for the pulsar and also the updated astrometric parameters for the runaway star, the minimal possible separation of 2.4 pc between the two stars is too large to be consistent with a common origin of both. Moreover, the closest approach of roughly 17 pc to Upper Scorpius of either of the two objects in all of the trajectories crossing within 10 pc makes it very unlikely that this region is the place of common origin.

However, the fraction of simulated orbits that cross within 10 pc (~8.6%) is surprisingly high and implies that the orbits of both objects may have crossed within that distance about 0.5 Myr ago. The allowed range in radial velocities for them to pass close by, on the other hand, is very small and points to a very strong kick imparted to the pulsar at birth. Only a direct measurement of the pulsar's radial velocity will further constrain the distance of closest approach of B1929+10 and ζ Oph.

Our data in combination with the updated astrometry for B1952+29 make a binary origin of B1929+10 and B1952+29 highly implausible.

5.2. Common origin of B2020+28 and B2021+51

Vlemmings et al. (2004) used the astrometric parameters from Brisken et al. (2002) (Table 4) to infer a putative common origin of B2020+28 and B2021+51. This conclusions seems plausible considering that the pulsars' 2D motions lie in apparently opposite directions in Galactic coordinates (Fig. 1 in Vlemmings et al. 2004) and also because the pulsars have very similar characteristic ages of 2.88 (B2020+28) and 2.75 Myr (B2021+51). Nevertheless, our new proper motion measurements, in conjunction with our parallax measurements, which place both pulsars almost twice as close as previous distance estimates, rule out a common origin for these two objects. Vlemmings et al. (2004) determined the percentage of orbits crossing within 10 pc for a known binary disrupted 1 Myr ago as a function of astrometric uncertainties (see their Fig. 2). These models indicate that our improved errors should have yielded 1% of crossing orbit realization (within 10 pc) for B2020+28 and B2021+51. However, in our simulations only 0.06% of trajectories cross within that distance, and none of the orbits yield an approach of less than 1.9 pc. Even if we use the bootstrapping results with their larger errors from Table 5, only 0.08% of the orbits cross within 10 pc. Furthermore, the orbits approaching each other within 10 pc do so at a median distance of $0.64^{+0.09}_{-0.11}$ kpc to the solar system. Given the estimated extent of the Cygnus Superbubble of 0.7–2.5 kpc (Vlemmings et al. 2004), a common origin within this region is ruled out.

5.3. Implications for Galactic electron density along the lines of sight

In Table 7 we list the distances inferred from our parallax measurements in comparison with those implied by the DM and
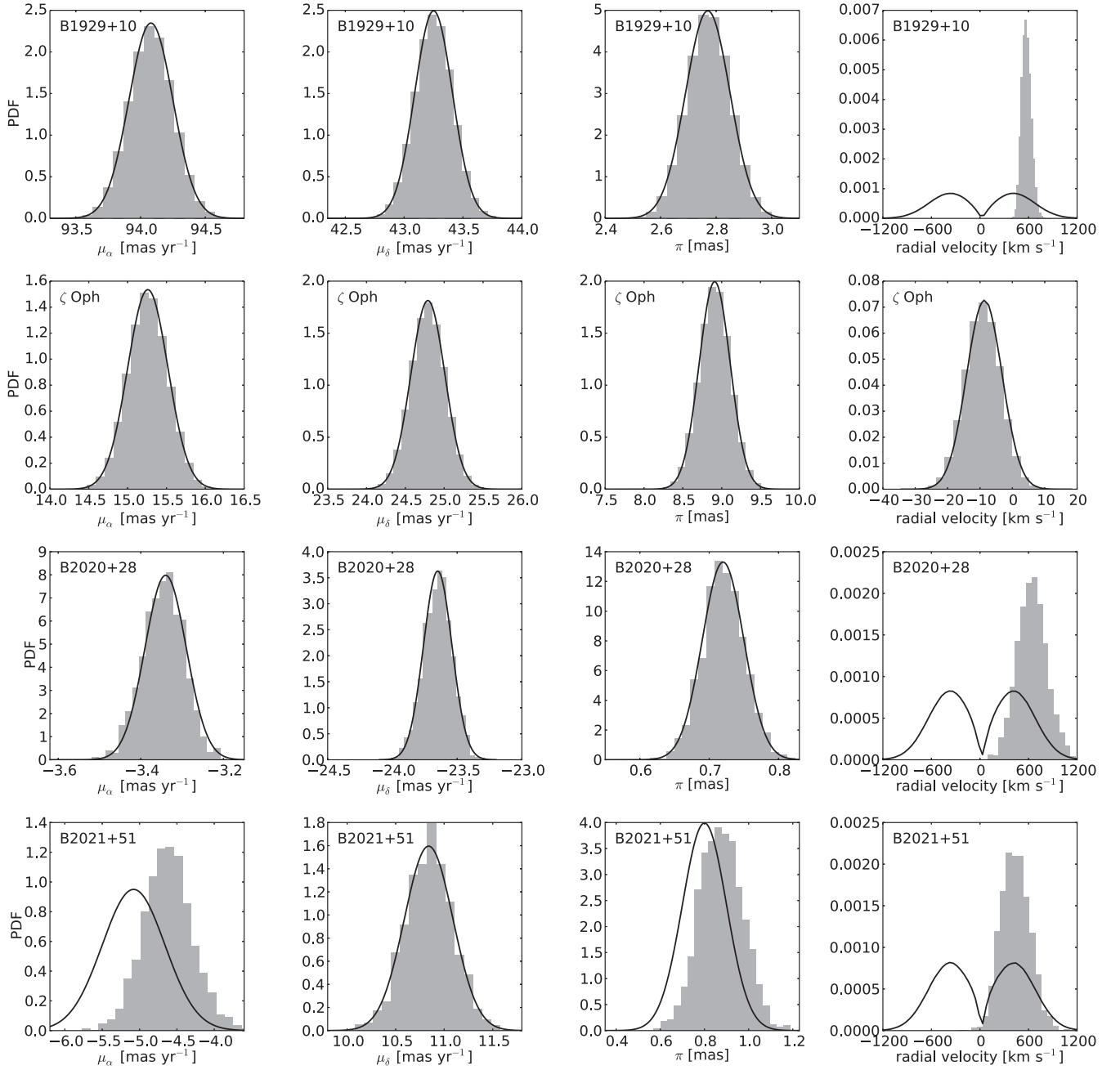
Fig. 7. Probability density function (grey histograms) of astrometric parameters and required radial velocities that result in a minimum separation of less than 10 pc between B1929+10/ζ Oph and B2020+28/B2021+51. Columns from *left to right* show the results for μ_α, μ_δ, π, and V_{rad}. For the measured parameters μ_α, μ_δ, and π, the solid lines indicate the input parameter distributions derived from assuming Gaussian errors. The solid line in the last column indicates the input distribution for V_{rad} as derived from our measured transverse velocity and the empirically determined space velocity distribution derived by Hobbs et al. (2005). Objects from *top to bottom* are B1929+10, ζ Oph, B2020+28, and B2021+51.

the Galactic electron density models of Cordes & Lazio (2003, NE2001) and Taylor et al. (1993, TC93, both obtained from the ATNF pulsar catalogue). While the NE2001–distance agrees with our measurement for B1929+10, the same model overestimates the distances to both B2020+28 and B2021+51 by a factor of about 1.5. The distance estimates for the latter two pulsars as given by the preceding model, TC93, agree well with our results, however. Hence, in combination with the DM as listed in Table 7, our parallax measurements imply a mean electron density of $8.8^{+0.3}_{-0.2}$, $17.7^{+0.8}_{-0.6}$, and $18.1^{+2.8}_{-1.8}$ cm^{-3} along the lines of sight to B1929+10, B2020+28, and B2021+51, respectively.

6. Conclusions

Based on our new astrometry for pulsars B1929+10, B2020+28, and B2021+51 obtained with the EVN at 5 GHz, we rule out previously proposed common origin scenarios for all three sources. Our Monte Carlo simulations of the past trajectory of B1929+10 throughout the Galactic potential show no indication for the pulsar to have once been in a binary system with the runaway star ζ Oph in Upper Scorpius. Similar simulations for B2020+28 and B2021+51 also rule out a binary origin of the pulsars in the Cygnus Superbubble.

Table 7. Parallax- vs. DM-based distances.

Source	DM [pc cm^{-3}]	$d_\pi{}^a$ [kpc]	$d_{\mathrm{NE2001}}{}^b$ [kpc]	$d_{\mathrm{TC93}}{}^c$ [kpc]
B1929+10	3.180 (4)	$0.361^{+0.009}_{-0.010}$	0.34	0.17
B2020+28	24.640 (3)	$1.39^{+0.05}_{-0.06}$	2.11	1.30
B2021+51	22.648 (6)	$1.25^{+0.14}_{-0.17}$	1.94	1.22

Notes. [a] Parallax-based distances derived in this work. [b] Distance estimate based on the Galactic electron density model from Cordes & Lazio (2003). [c] Distance estimate based on the Galactic electron density model from Taylor et al. (1993). Except for d_π, all values were taken from the ATNF pulsar catalogue.

References

Arzoumanian, Z., Chernoff, D. F., & Cordes, J. M. 2002, ApJ, 568, 289
Bobylev, V. V. 2008, Astron. Lett., 34, 686
Brisken, W. F., Benson, J. M., Goss, W. M., & Thorsett, S. E. 2002, ApJ, 571, 906
Chatterjee, S., Cordes, J. M., Lazio, T. J. W., et al. 2001, ApJ, 550, 287
Chatterjee, S., Cordes, J. M., Vlemmings, W. H. T., et al. 2004, ApJ, 604, 339
Cordes, J. M., & Chernoff, D. F. 1998, ApJ, 505, 315
Cordes, J. M., & Lazio, T. J. W. 2003, ArXiv e-prints [arXiv:astro-ph/0301598]
de Zeeuw, P. T., Hoogerwerf, R., de Bruijne, J. H. J., Brown, A. G. A., & Blaauw, A. 1999, AJ, 117, 354
Famaey, B., & Dejonghe, H. 2003, MNRAS, 340, 752
Hobbs, G., Lyne, A. G., Kramer, M., Martin, C. E., & Jordan, C. 2004, MNRAS, 353, 1311
Hobbs, G., Lorimer, D. R., Lyne, A. G., & Kramer, M. 2005, MNRAS, 360, 974
Hobbs, G. B., Edwards, R. T., & Manchester, R. N. 2006, MNRAS, 369, 655
Hoogerwerf, R., de Bruijne, J. H. J., & de Zeeuw, P. T. 2001, A&A, 365, 49
Keimpema, A., Kettenis, M. M., Pogrebenko, S. V., et al. 2015, Exp. Astron., in press [arXiv:1502.00467]
Kettenis, M., van Langevelde, H. J., Reynolds, C., & Cotton, B. 2006, in Astronomical Data Analysis Software and Systems XV, eds. C. Gabriel, C. Arviset, D. Ponz, & S. Enrique, ASP Conf. Ser., 351, 497
Kharchenko, N. V., Scholz, R.-D., Piskunov, A. E., Röser, S., & Schilbach, E. 2007, Astron. Nachr., 328, 889
Kovalev, Y. Y., Lobanov, A. P., Pushkarev, A. B., & Zensus, J. A. 2008, A&A, 483, 759
Ma, C., Arias, E. F., Bianco, G., et al. 2009, IERS Technical Note, 35, 1
Peck, L. W., & Fenech, D. M. 2013, Astron. Comput., 2, 54
Porcas, R. W. 2009, A&A, 505, L1
Scheck, L., Kifonidis, K., Janka, H.-T., & Müller, E. 2006, A&A, 457, 963
Schönrich, R. 2012, MNRAS, 427, 274
Sokolovsky, K. V., Kovalev, Y. Y., Pushkarev, A. B., & Lobanov, A. P. 2011, A&A, 532, A38
Taylor, J. H., & Cordes, J. M. 1993, ApJ, 411, 674
Taylor, J. H., Manchester, R. N., & Lyne, A. G. 1993, ApJS, 88, 529
Tetzlaff, N., Neuhäuser, R., Hohle, M. M., & Maciejewski, G. 2010, MNRAS, 402, 2369
van Leeuwen, F. 2007, A&A, 474, 653
Vlemmings, W. H. T., van Langevelde, H. J., Diamond, P. J., Habing, H. J., & Schilizzi, R. T. 2003, A&A, 407, 213
Vlemmings, W. H. T., Cordes, J. M., & Chatterjee, S. 2004, ApJ, 610, 402
Wright, G. A. E. 1979, Nature, 277, 363